PAPER

Check for updates

Effect of spectrin network elasticity on the shapes of erythrocyte doublets†

Masoud Hoore, [a] François Yaya, [bc] Thomas Podgorski, [c] Christian Wagner, [bd] Gerhard Gompper [a] and Dmitry A. Fedosov *[a]

Red blood cell (RBC) aggregates play an important role in determining blood rheology. RBCs in plasma or polymer solution interact attractively to form various shapes of RBC doublets, where the attractive interactions can be varied by changing the solution conditions. A systematic numerical study on RBC doublet formation is performed, which takes into account the shear elasticity of the RBC membrane due to the spectrin cytoskeleton, in addition to the membrane bending rigidity. RBC membranes are modeled by two-dimensional triangular networks of linked vertices, which represent three-dimensional cell shapes. The phase space of RBC doublet shapes in a wide range of adhesion strengths, reduced volumes, and shear elasticities is obtained. The shear elasticity of the RBC membrane changes the doublet phases significantly. Experimental images of RBC doublets in different solutions show similar configurations. Furthermore, we show that rouleau formation is affected by the doublet structure.

1 Introduction

In whole blood, red blood cells (RBCs) experience a pronounced attractive interaction, which is mediated by plasma proteins such as fibrinogen.[1,2] Similar attraction between RBCs is also observed in solutions of dextran[3–5] or other macromolecules. Such an attractive interaction leads to the formation of RBC aggregates, in particular large rouleaux, which play an essential role in the strong shear-thinning behavior of blood at low and moderate shear rates.[6–8] Thus, the interaction of RBCs with each other and with adhesive surfaces is of great interest to understand the rheology of blood and rouleau formation. The first step for studying RBC assembly into rouleaux is an aggregate of two RBCs, called a doublet. The formation and shape of RBC doublets is determined by the competition between bending and shear elasticity, and the adhesion energy.

The RBC membrane has a characteristic biconcave shape, which can be well described by the Helfrich bending elasticity[9,10] similar to fluid vesicles, whose shape is determined by the bending free energy and volume and area conservation of a closed membrane.[11,12] However, in addition to bending resistance, RBC membranes possess a shear elasticity supplied by their spectrin cytoskeletal network, which differentiates them from lipid vesicles.[13–15]

The first theoretical studies[16–18] of RBC doublets considered a flat shape for the contact surface between RBCs to simplify the analysis. Later, numerical studies have shown that two fluid vesicles with bending rigidity and constant volume form a curved contact surface.[19–21] Different shapes of vesicle doublets as a function of their adhesion strength and bending rigidity were predicted. These shapes are also qualitatively consistent with those obtained in several two-dimensional (2D) investigations.[22–24] In recent work,[25] various RBC doublet phases have been explored depending on the dextran and fibrinogen concentration, which modifies the attractive interaction between RBCs. The experimental data have been mainly supported by two-dimensional (2D) simulations,[25] and therefore, it remains unclear whether the whole phase space of the system has been explored or not and whether some other RBC doublet phases exist in practice. Furthermore, another interesting question is how the shear elasticity of the RBC membrane affects different doublet phases, since previous investigations[19,20] have primarily focused on bending rigidity. Similar issues are important for the complexation of vesicles with particles of similar size, such as colloidal particles or other vesicles,[26] as well as for similar complexes of RBCs with other micro-particles.

a Theoretical Soft Matter and Biophysics, Institute of Complex Systems and Institute for Advanced Simulation, Forschungszentrum Jülich, 52425 Jülich, Germany. E-mail: d.fedosov@fz-juelich.de

b Experimental Physics, Saarland University, 66123 Saarbrücken, Germany

c Laboratoire Interdisciplinaire de Physique, CNRS and Université Grenoble Alpes, 140 rue de la Physique, 38402 Saint-Martin d'Hères, France

d Physics and Materials Science Research Unit, University of Luxembourg, Luxembourg

† Electronic supplementary information (ESI) available: Movie S1 illustrates the performance of two different discretizations (KN and GK) of the Helfrich bending energy from eqn (1) for a fluid vesicle in equilibrium. The KN model fails to properly capture the characteristic biconcave shape in equilibrium, while the GK model leads to the biconcave resting shape. Movie S2 demonstrates the formation of RBC doublets for different shear moduli and reduced adhesion strengths. See DOI: 10.1039/c8sm00634b

Here, we systematically study the phase space of RBC doublets using simulations of high resolution triangulated membranes with bending and shear elasticity in three dimensions (3D). Specifically, we focus on the effect of membrane shear elasticity in determining different RBC doublet phases and find that a change in RBC shear elasticity significantly modifies the doublet phase space. Furthermore, we explore the influence of the RBC reduced volume on doublet shapes. The various phases of RBC doublets, predicted theoretically, are also compared with experimental results.

2 Methods & models

2.1 Membrane model

The RBC membrane is represented by a triangular mesh, as described in detail in ref. 27–30. The important energies for RBC doublets are the bending energy from the lipid bilayer and the shear elasticity of the spectrin network, and the adhesive energy between the two RBCs. The bending energy for fluid membranes, which do not possess a preferred radius of curvature, reads[9,31–34]

$$U_b = \frac{1}{2}\kappa_c \oint_A dA(c_1 + c_2)^2 + \kappa_g \oint_A dA c_1 c_2, \qquad (1)$$

where κ_c, κ_g, c_1, and c_2 are the bending rigidity, the Gaussian bending modulus, and principal curvatures of the membrane, respectively. The energy is integrated over the whole membrane area A enclosing the volume V. The integral over the Gaussian curvature $K = c_1 c_2$ is constant for a fixed topology, due to the Gauss–Bonnet theorem.[32,34]

The simplest discretization of the bending energy in eqn (1) has been proposed by Kantor & Nelson (KN)[35] for every pair of adjacent triangles,

$$U_{KN} = \sum_{i,j} \kappa_b (1 - \mathbf{n}_{ijk} \cdot \mathbf{n}_{ijk'}), \qquad (2)$$

where κ_b is the bending constant, and $\mathbf{n}_{ijk}$ is the unit normal vector of the triangle with vertices i, j, and k (see Fig. 1). The quantity κ_b is related to the bending rigidity κ_c as $\kappa_c = \kappa_b \sqrt{3}/2$ for a sphere in the continuum limit.[28,32,36,37] Even though such a discretized bending model for RBCs has been quite successful in predicting RBC behavior, including membrane fluctuations,[38] RBC mechanical properties,[27–29] and flow dynamics,[39,40] it is not accurate enough if the bending energy of the membrane dominates. A similar conclusion has been also reached in a recent investigation,[41,42] where different discretizations of the bending energy were tested.

A more accurate discretization for the bending energy has been proposed by Gompper & Kroll (GK)[32] as

$$U_{GK} = \frac{1}{2}\kappa_c \sum_i \frac{1}{\sigma_i} \left(\sum_{j(i)} \sigma_{ij} \hat{r}_{ij} \right)^2, \qquad (3)$$

where $\sigma_i = \frac{1}{4}\sum_{j(i)} \sigma_{ij} r_{ij}$, $\sigma_{ij} = r_{ij}(\cot\theta_k + \cot\theta_{k'})/2$, r_{ij} is the distance from vertex i to j, $\hat{r}_{ij}$ is the unit vector pointing to vertex i from j,
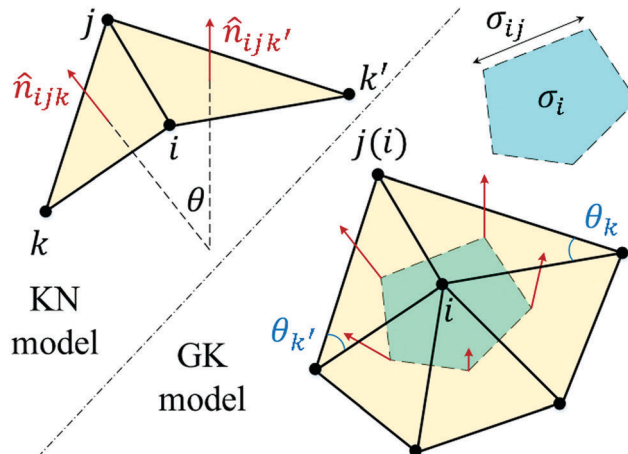

Fig. 1 Schematic of the two discretization models for the bending energy. The KN discretization[35] in eqn (2) considers the bending of each adjacent triangle pair, while the GK discretization[32] in eqn (3) represents the bending of each vertex with respect to all of its linked vertices.

$j(i)$ are the vertices connected to vertex i by bonds, and θ_k and $\theta_{k'}$ are the angles opposite to the bond between vertex i and j in triangles ikj and $ik'j$ (see Fig. 1). σ_i and σ_{ij} are the area of each cell and the length of each bond, respectively, in the dual lattice of the triangulated lattice of the membrane,[32] as shown in Fig. 1. Different discretization models have been explained in more detail in ref. 41–43.

The membrane elasticity due to the spectrin bonds is represented by a combination of the worm-like chain (WLC) and power (POW) potentials, as described in ref. 28 and 29. The network model of the membrane conserves its global surface area and volume by harmonic constraint potentials with stiffnesses k_a and k_v, respectively.[28,29] The local area of each triangle is also softly constrained by a harmonic potential with a stiffness k_l.[28,29] The Young's and shear moduli are derived from the WLC potential and the area conservation potentials, as described in ref. 29, 50 and 51. Since our main interest is in final doublet configurations in equilibrium, which are determined by a minimum of the energies involved, dynamic effects do not contribute and the effect of membrane and fluid viscosities can be neglected. In simulations, the motion of membranes is governed by Langevin dynamics.[52] It is worth mentioning that our simulation approach includes thermal fluctuations, which, however, are of minor importance for doublet shapes. The membrane properties of RBCs are provided in Table 1.

In order to test the performance of the two discretization schemes for bending energy, we model the equilibrium shape of a fluid vesicle with a reduced volume $\nu = 3V/4\pi R_s^3 = 0.64$, where $4\pi R_s^2 = A$. For this value of the reduced volume, the vesicle must attain a biconcave shape,[53] which is also the equilibrium shape of RBCs.[44] Here, A and V correspond to the membrane area and volume, respectively. Note that the shape of a vesicle is determined by the bending energy and the reduced volume.[11,12,53] By removing the shear elasticity from the membrane model (i.e. omitting the bond potential), we find

Table 1 Membrane properties used in simulations and related references

Property (units)	Value (variability)
Number of vertices, N	3000
Surface area, A (μm^2)	134[28,29,44,45]
Volume, V (μm^3)	94[28,29,44,45]
Effective diameter, $D_{\text{eff}} = \sqrt{A/\pi}$ (μm)	6.5
Bending rigidity, $\kappa_c/k_B T$	70[28,29]
Shear modulus, G (μN m^{-1})	4.6 (2–12)[29,46–49]
Global area rigidity, $k_a D_{\text{eff}}^2/\kappa_c$	29 600[28,29]
Local area rigidity, $k_l D_{\text{eff}}^2/\kappa_c$	603[28,29]
Global volume rigidity, $k_v D_{\text{eff}}^3/\kappa_c$	19 620[28,29]

KN Model $\sum_{i,j} \kappa_b (1 - \vec{n}_{ijk} \cdot \vec{n}_{ijk'})$

GK Model $\frac{1}{2} \kappa_c \sum_i \frac{1}{\sigma_i} \left(\sum_{j(i)} \sigma_{ij} \hat{r}_{ij} \right)^2$
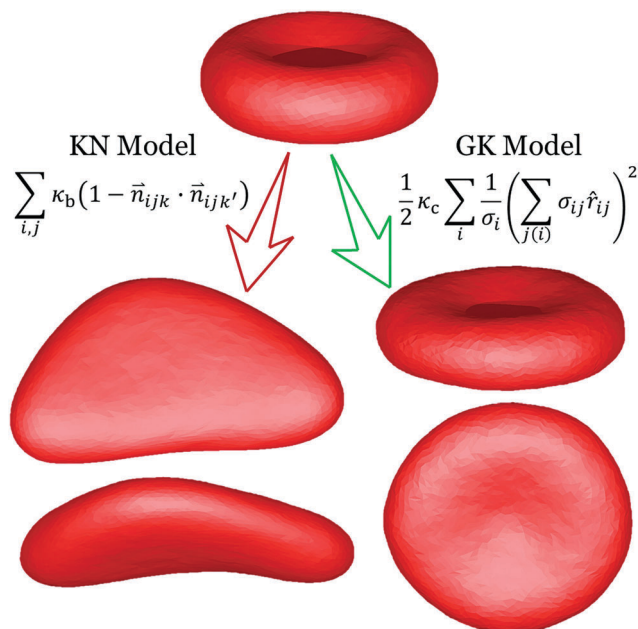
Fig. 2 Vesicle shapes from the two discretization schemes of the bending energy. The elastic bond (spring) potential is turned off, so that no shear elasticity is present. The standard biconcave shape of a RBC is maintained if the discretization is based on the GK scheme. The KN scheme fails to keep the RBC biconcave shape (see Movie S1, ESI†).

that the KN discretization from eqn (2) does not preserve the initial biconcave shape of the membrane (see Fig. 2 and Movie S1, ESI†), indicating that this state does not remain the equilibrium point for the membrane. In contrast, the GK discretization from eqn (3) successfully keeps the biconcave shape without the spectrin network elasticity, as shown in Fig. 2 and Movie S1 (ESI†). The shear elasticity of the RBC membrane from the spectrin network partially compensates for the inaccuracy of the KN model; however, the GK model is clearly more accurate and is employed in this work.

2.2 Adhesion model

To represent aggregation between two RBCs, attractive interactions between two membranes are introduced, similar to other models[19,20,25,54] of interacting membranes. Note that such interactions cannot be directly associated with any underlying mechanism for RBC aggregation (e.g. depletion or bridging). Therefore, this model constitutes an effective representation of

the aggregation between RBCs, which is characterized by the strength of the attractive interaction and the contact area.

The attractive interaction between adjacent vertices of membranes in contact is modeled by the Lennard-Jones (LJ) potential

$$U_{\text{LJ}}(r) = 4\varepsilon \left[\left(\frac{\sigma}{r} \right)^{12} - \left(\frac{\sigma}{r} \right)^6 \right], \quad (4)$$

where ε and σ are the energy and characteristic length of the LJ interaction. The LJ potential is cut off at $r_{\text{cut}} = 2.5\sigma$.

The contact interaction of two RBCs can be represented by the adhesion free energy[19,20]

$$E_{\text{adh}} = -\Gamma A_c, \quad (5)$$

where Γ is the adhesion strength and A_c is the contact area. Providing that the adhesion is modeled by a pairwise interaction, such as the LJ potential in eqn (4), between membrane vertices, the adhesion strength Γ can be related to the potential energy ε. If N_c vertices from one RBC interact with the vertices from another RBC, the total adhesion energy is $-N_c\tilde{\varepsilon}$, where $\tilde{\varepsilon}$ is the effective adhesion energy of one RBC vertex with the other RBC vertices. $\tilde{\varepsilon}$ can be calculated approximately by considering the closest vertices to a vertex from another membrane, as illustrated in Fig. 3. In a minimal energy state, a vertex sits on top of three vertices in a tetrahedral configuration with equal distance σ to all of them. The adhesion energy of this vertex with the other closest neighbors sums to about -5.37ε. Consequently, the total adhesive energy, when N_c vertices participate in the adhesion from each membrane, is equal to about $-5.4N_c\varepsilon$. However, this high symmetry situation of course does not occur for all of the vertices, resulting in a somewhat smaller adhesion energy. As vertices of a membrane are homogeneously distributed on the membrane, $N_c/A_c = N/A$, in which N and A are the total number of vertices and the total area of the RBC membrane. Thus, the adhesion strength is directly proportional to the vertex density N/A, i.e. $\Gamma = N_c\tilde{\varepsilon}/A_c = N\tilde{\varepsilon}/A$. This implies that the adhesion strength is proportional to the LJ parameter ε via $\tilde{\varepsilon}$.

The reduced adhesion energy, γ, is defined as the ratio of the total possible adhesion energy (i.e. when $A_c = A$) to the bending energy of a sphere,

$$\gamma = \frac{\Gamma A}{8\pi\kappa_c} = \frac{N\tilde{\varepsilon}}{8\pi\kappa_c}. \quad (6)$$

The ratio $\tilde{\varepsilon}/\varepsilon$ as a function of γ and reduced volume ν ($\nu_1 = \nu_2 = \nu$) is presented in Fig. 4, which shows how the effective adhesion energy $\tilde{\varepsilon}$ is related to the pairwise LJ energy ε. For different ε values, the equilibrium distance between the two membranes may change, leading to a different relation between ε and $\tilde{\varepsilon}$. This is the main reason for an increase in $\tilde{\varepsilon}/\varepsilon$ with decreasing γ. A very weak dependence of $\tilde{\varepsilon}/\varepsilon$ on the reduced volume ν can be due to the local curvature of contact. Additionally, for large enough ν, membranes in a doublet configuration are under tension, which may contribute to the dependence of the ratio $\tilde{\varepsilon}/\varepsilon$ on ν. Finally, the amplitude of thermal fluctuations of a RBC membrane is known to be spatially non-uniform along the
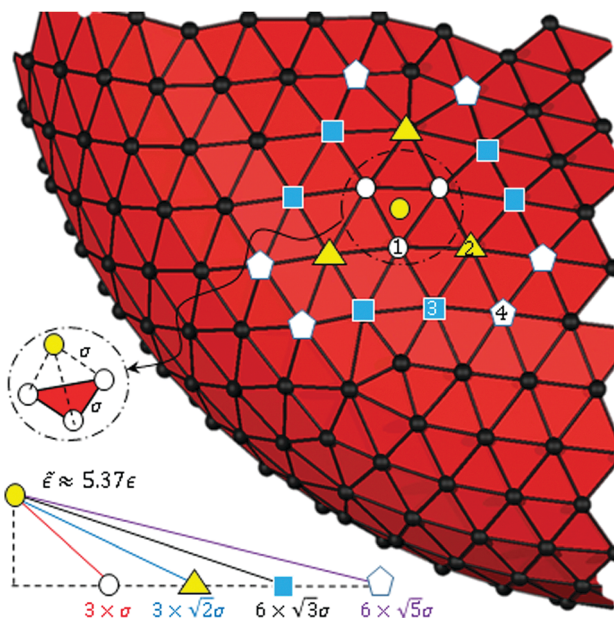
Fig. 3 Analysis of the contact area and the approximation of adhesion energy. The minimum adhesion energy for a vertex is obtained when it is located at the head of an equilateral tetrahedron, one of whose faces is the triangle of the other membrane vertices. The four closest neighbors to this vertex are shown by different symbols with assigned numbers 1–4. The closest neighbors are 3 vertices with distance σ, and the second closest neighbors are again 3 vertices approximately $\sqrt{2}\sigma$ away from this vertex. Also 6 neighbors with a $\sqrt{3}\sigma$ and 6 other with a $\sqrt{5}\sigma$ distance are the farthest neighbors, which affect the adhesion energy. Even further neighbors have a negligible effect on the energy and are ignored. Thus, the effective adhesion energy $\tilde{\varepsilon}$ of one interacting vertex is equal to about 5.37ε. In another configuration, where a vertex sits close to only one vertex from the other membrane, the effective adhesion energy would be approximately 4.1ε.
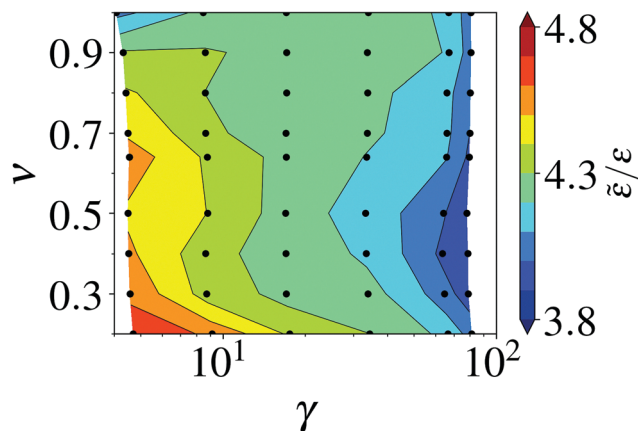
Fig. 4 The ratio of the effective adhesion energy $\tilde{\varepsilon}$ to the pairwise energy ε. This ratio depends weakly on the configuration of the two adhered RBCs, as illustrated in Fig. 3. Simulations are conducted for the system until it reaches equilibrium. The reported data are averaged over 250 uncorrelated points in simulations from the equilibrium states. On average, $\tilde{\varepsilon}/\varepsilon = 4.23 \pm 0.03$.

surface,[55,56] and to depend on the membrane shape, local curvature, and tension.[57] Membrane thermal fluctuations are

included in the model (see Movie S2, ESI†) and would effectively introduce short-range repulsion between two membranes.

2.3 Experiments

Blood was obtained by finger pricking from healthy donors after giving informed consent in compliance with the ethical requirements of Saarland University, Saarbrücken, Germany (Ärztekammer des Saarlandes, approval number 24/12). RBCs were washed twice with Phosphate Buffered Saline (PBS, 290 mOsm) following the standard procedure.[58] Then, RBCs were resuspended in several solutions to obtain several doublet configurations. In order to have various adhesion energies,[4] we prepared dextran solutions with different molecular weights:

• 40 kDa at a concentration of 10 mg ml^{-1} with an adhesion energy close to 1 μJ m^{-2};

• 70 kDa at a concentration of 20 mg ml^{-1} with an adhesion energy close to 4 μJ m^{-2};

• 500 kDa at a concentration of 10 mg ml^{-1} with an adhesion energy close to 6 μJ m^{-2}.

Fibrinogen was added with a concentration of 6 mg ml^{-1} to autologous plasma as it does not induce spontaneous aggregation on its own. A hypotonic solution of NaCl at 0.6% was also prepared to increase the RBC volume. To induce aggregation, dextran 70 kDa was added with a concentration of 50 mg ml^{-1} into this solution. The hematocrit level was kept at 0.5% in every sample. Such a low concentration of RBCs allows us to manipulate cells freely with holographic optical tweezers. Then, cells were held at their edge with four optical traps. RBCs were brought together to form doublets and the traps were released, so that they can spontaneously aggregate. As dextran is known to induce spontaneous aggregation,[59] we observe the formation of rouleaux over time. Finally, RBCs were allowed to sediment for 30 min and micro-photographs were taken using a 60-fold objective. Morphologies of these aggregates were characterized similarly to those in the simulations.

3 Doublet shapes

The theoretical adhesion strength Γ is related to dextran and fibrinogen concentrations in experiments.[59,60] RBC doublet shapes are determined by the adhesion strength (Γ, or equivalently γ), the reduced volumes ν_1 and ν_2, and the elastic parameters such as bending rigidity κ_c and shear elasticity G. The adhesion strength of the RBC membranes is about 1 μJ m^{-2} in plasma and about 10 μJ m^{-2} in dextran solutions,[61] corresponding to $\gamma \approx 4$ in plasma and $\gamma \approx 40$ in dextran. The RBC volume is also subject to change in different solutions, and may also vary from one cell to the other.

Fig. 5 shows doublet conformations, the contact area, and the bending energy for various $\nu_1 = \nu_2 = \nu$ and γ. The contact area A_c is normalized by the RBC area A. The bending energy E_b is calculated directly from simulations and normalized by the bending energy $8\pi\kappa_c$ of a sphere,

$$\varepsilon_b = \frac{E_b}{8\pi\kappa_c}, \qquad (7)$$

where ε_b denotes the reduced bending energy.
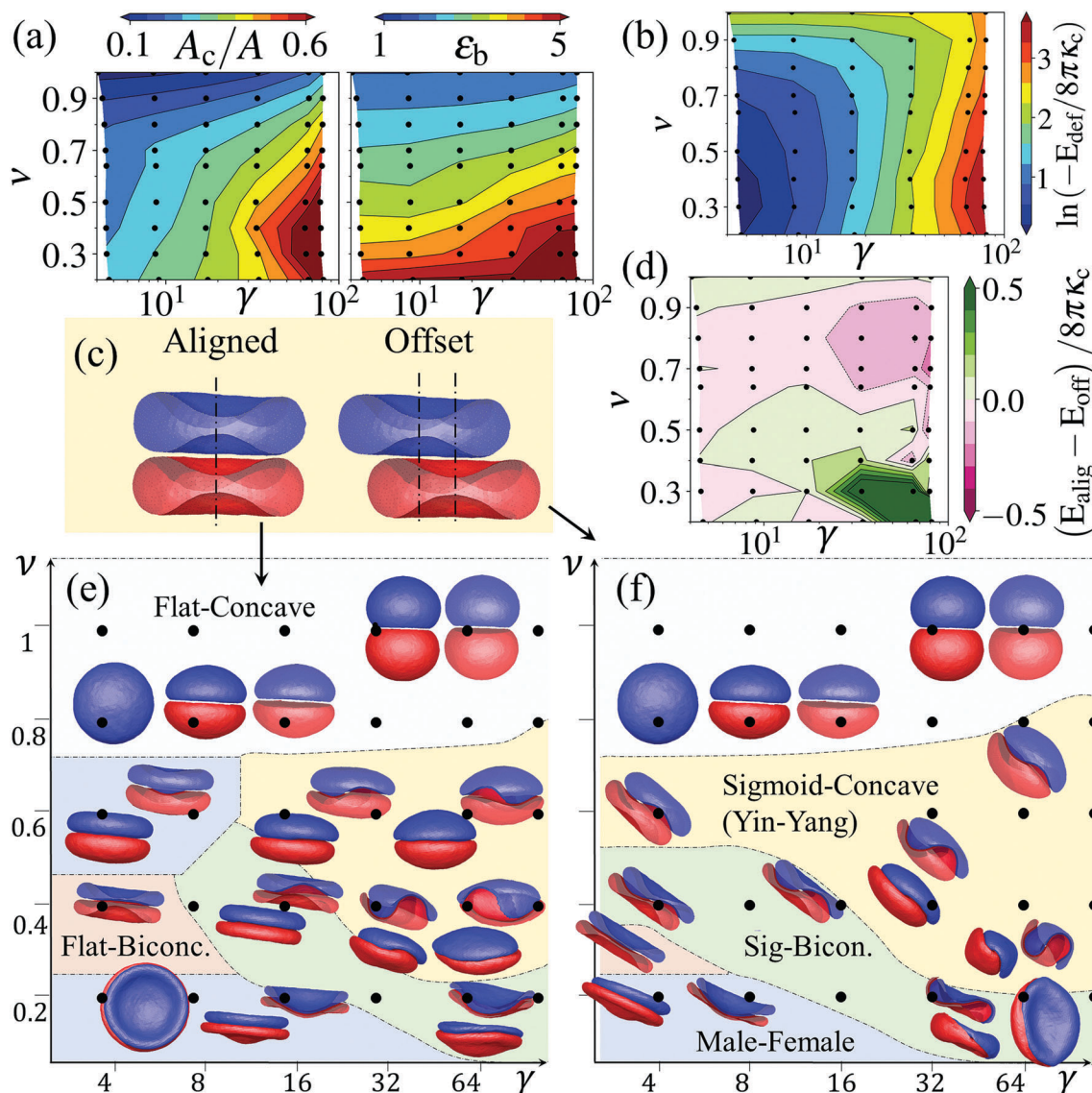
Fig. 5 RBC doublet configurations as a function of $\nu_1 = \nu_2 = \nu$ and γ with aligned and offset first points of contact. (a) Contour plots for the contact area and the reduced bending energy for the aligned RBCs. (b) Contour plot for the difference between the free energy of the doublet and the free RBCs (the deformation energy). The change in free energy is normalized by the bending energy of a vesicle with bending modulus κ_c, $8\pi\kappa_c$, and the colorbar has a logarithmic scale. The black dots (•) in contour plots represent the values for which simulations have been conducted. (c) The configuration of a doublet depends on the way the RBCs make their first contact. RBCs can make the first contact while they are in aligned or offset configurations. (d) The difference between the free energy of the doublets in the aligned and offset cases. If $E_{\text{alig}} - E_{\text{off}}$ is positive, it means that the offset doublet has a smaller free energy, so that it is a more favorable configuration. The phase diagrams of the (e) aligned and (f) offset cases are different in the region where $E_{\text{alig}} - E_{\text{off}}$ is positive. Various phases are distinguished by their cross-sectional views. The black dots (•) in the phase diagrams represent performed simulations. Note that the phase boundaries are drawn schematically to guide the eye.

The contact area is more sensitive to the reduced adhesion strength and the bending energy is more sensitive to the reduced volume, see Fig. 5(a). Overall, as the reduced volume decreases and the adhesion strength increases, both the contact area and the membrane bending energy increase.

The configurations both for the initially aligned and for the offset doublets (Fig. 5(c)) are depicted in Fig. 5(e) and (f). The phases of RBC doublets for the initially aligned and offset configurations match at high adhesion strengths or high reduced volumes. However, a mismatch of doublet phases is

observed for low adhesion strengths and low reduced volumes, see Fig. 5(d)–(f). This indicates the existence of several local minima in the free-energy landscape, making the first point of contact important for RBC doublets. Multiple local minima in the free-energy should also exist for fluid vesicles, even though this has not been demonstrated so far. In comparison to vesicles, RBCs also possess an elastic spectrin network, which may have anisotropic local pre-stress. This additional property likely contributes to a complex energetic landscape for RBC doublets with several metastable states or local minima.

Various phases can be distinguished, as illustrated in Fig. 5(e) and (f). All observed shapes are categorized by their contact surface and their non-adhered free surfaces, as follows:

• Male–female (M–F) phase: both RBCs attain a cup shape and plug into each other similar to the male and female terminals of a socket. The M–F phase provides the highest contact surface at the cost of bending energy, so that the total energy is minimized.

• Sigmoid–concave (Yin–Yang) phase: the RBCs make a sigmoid contact area, which is different from the native sigmoid (concave) shape of a RBC membrane. This condition occurs at high adhesion strengths, since the bending free energy of the RBCs increases substantially, but is compensated for by the decrease in the adhesion energy. Since the cross-sectional view of the sigmoid–concave shape looks similar to the Yin–Yang symbol, we also call it the Yin–Yang phase.

• Sigmoid–biconcave (S–B) phase: this phase is located between the Yin–Yang and M–F phases. The RBCs are attached to each other in such a way that the concave part of one RBC fills the convex part of the other. In other words, the contact surface is sigmoid, while the free surface remains biconcave.

• Flat–concave (F–C) phase: if both RBCs are swollen, the M–F phase becomes unstable and both RBCs reconcile by making a flat contact surface and keeping their free surfaces near spherical. This phase appears at large reduced volumes.

• Flat–biconcave (F–B) phase: this phase with a flat contact area and remaining concavities at the free surfaces is obtained for $\nu_1 = \nu_2 \approx$ 0.3–0.4 and $\gamma \lesssim 8$ when the RBCs align with no offset. Fig. 5(e) and (f) show that the F–B phase shrinks to a very small region if the RBCs are initially in contact with an offset. Thus, the F–B phase is less probable to be seen under physiological conditions, where the offset contact is far more probable than the aligned contact.

Although the F–B phase is the stable doublet configuration for the aligned doublets, the bending energy at this state is not at a global minimum. It can be seen from the free energy difference between the aligned and offset configurations in Fig. 5(d). Under physiological conditions ($\nu \approx 0.64$), the M–F phase can be observed when the RBCs make the first contact in an aligned configuration, which is unlikely to be observed experimentally.

Fig. 6 illustrates various doublet shapes of two RBCs with different reduced volumes for a fixed reduced adhesion energy $\gamma = 8$. Another phase, the sheath phase, appears here.

• Sheath phase: if the reduced volume of one RBC is large, and that of the other is small, the former would swell to an elliptical shape and the latter would bend to a cup shape. Therefore, the best configuration for their adhesion occurs when the inner cup of the latter RBC matches the swollen curvature of the former RBC. This configuration corresponds to the minimal free energy condition for almost all adhesion strengths. Since most RBCs have a reduced volume in the range 0.4 to 0.8, such a phase does not occur under physiological conditions.

In the case of unequal reduced volumes (see Fig. 6), the contact area is roughly proportional to the inverse of the
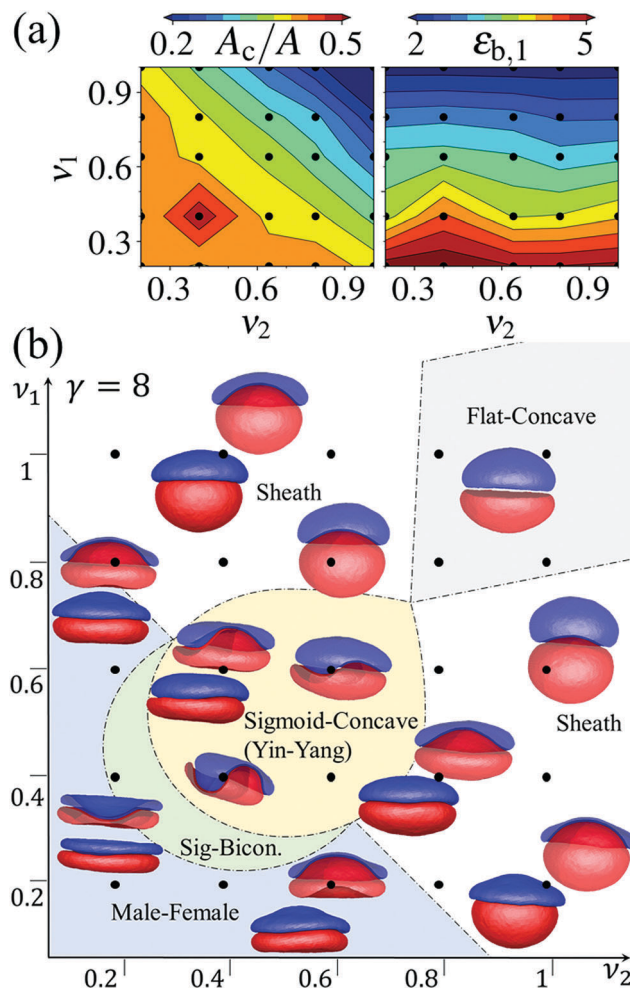

Fig. 6 RBC doublet configurations as a function of ν_1 and ν_2 at a constant adhesion strength $\gamma = 8$. (a) Contour plots show the contact area and the reduced bending energy of the first RBC as a function of ν_1 and ν_2. The black dots (•) represent the values for which simulations have been performed. (b) The side and section views of some configurations are shown in the phase diagram, omitting some shapes for more clarity. The different phases are separated by different colors. The S−B phase occurs in a narrow region between the Yin−Yang and M−F phases. The membrane is assumed to be stress-free in its biconcave shape with $\nu = 0.64$. The phase boundaries are drawn schematically to guide the eye.

average of the reduced volumes $(A_c/A \propto (\nu_1 + \nu_2)^{-1})$ and varies from about 0 to 0.7. The reduced bending energy $\varepsilon_{b,1}$ of the first RBC decreases with increasing ν_1, but is not very sensitive to a variation in the reduced volume ν_2 of the second RBC.

In order to study the effect of the spectrin network's shear elasticity on the doublet phases, the membrane shear modulus G is varied. Fig. 7 shows the phase diagram together with the contact area and reduced bending energy as a function of shear modulus and adhesion strength for a constant reduced volume of healthy RBCs $\nu \approx 0.64$. The shear modulus of healthy RBCs lies in the range 2–12 μN m^{-1},[29,46–49,62] which corresponds to a reduced shear modulus $\mu = GA/8\pi\kappa_c$ of 35–215, provided that the bending rigidity is 70 $k_B T$. The phases obtained for very low shear moduli agree well with the numerical energy-minimization study for vesicles,[19] where the contact area is flat
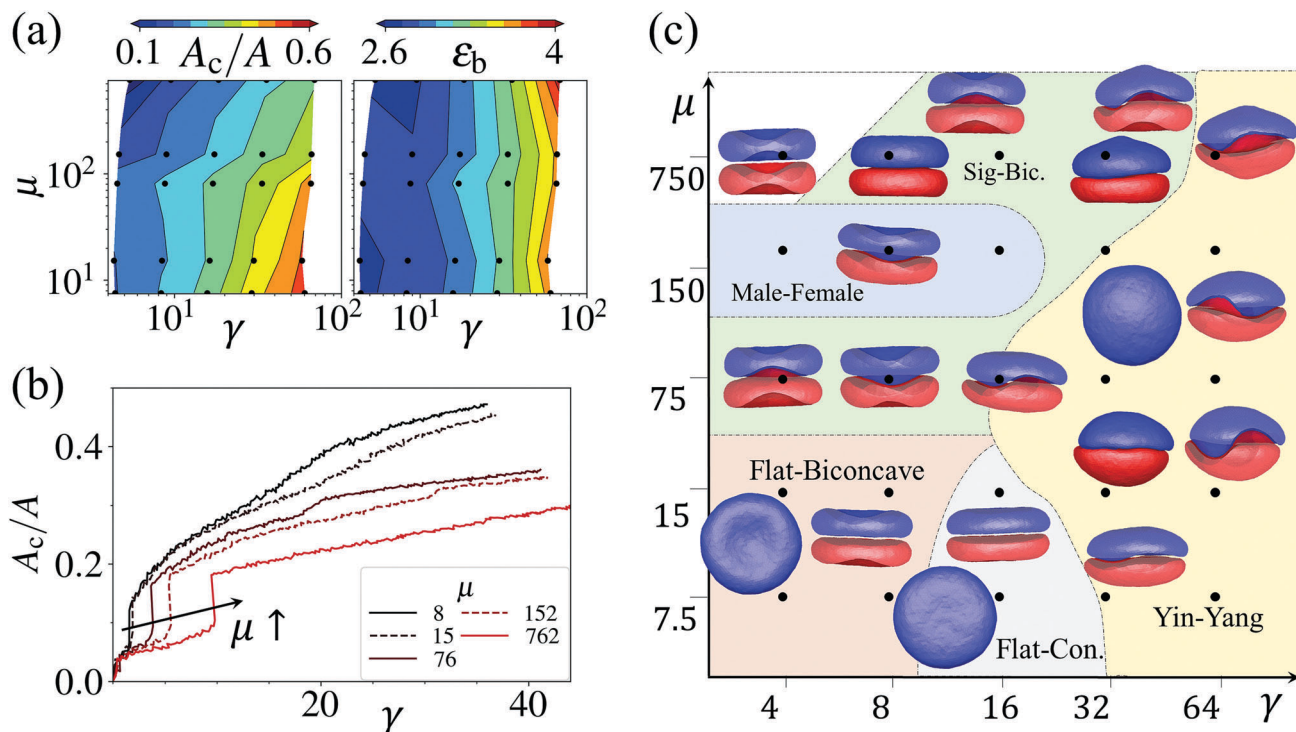
Fig. 7 RBC doublet configurations as a function of the spectrin network's reduced shear modulus $\mu = GA/8\pi\kappa_c$ and reduced adhesion strength γ at a constant reduced volume $\nu = 0.64$. (a) Contour plots show the contact area and the reduced bending energy. The black dots (●) represent the values for which simulations have been performed. (b) Dependence of the contact area on adhesion strength for different μ values. A discontinuity in the contact area is observed when one or both RBCs lose their original biconcave shape. (c) Phase diagram of RBC doublets as a function of γ and μ, where different phases are separated by various colors. The phase boundaries are drawn schematically to guide the eye. The side and section views of some configurations are shown, omitting some shapes for more clarity. The low shear moduli approximate vesicle doublets. The membrane is assumed to be stress-free in its biconcave shape with $\nu = 0.64$.

for low adhesion strengths and it buckles as the adhesion strength increases. The F–B phase appears in a broader range of adhesion strengths when the shear modulus is much lower than that for a healthy RBC. Also, the F–C phase, which has never been detected for normal RBC reduced volumes of $\nu \approx 0.64$, appears at very low shear moduli. On the other hand, at shear moduli of healthy RBCs, the M–F and S–B phases are found at low adhesion strengths. If the shear modulus is very high, the RBCs do not tend to form the contact area from their center. A high shear modulus is relevant for diseased RBCs, such as in malaria.[63]

The doublet phases are determined by the balance of deformation energies and adhesion energy. The shear elasticity of the membrane attributed to the spectrin network has a strong effect on the doublet phases, as shown in Fig. 7. For vesicle doublets, the effect of shear elasticity is absent since vesicles are made of a fluid membrane. Accordingly, the lower region of the phase diagram ($\mu \to 0$) in Fig. 7 corresponds to the previous work on doublets with the three phases F–C, F–B, and sigmoid–concave (Yin–Yang),[19,20,25,54] characterized by the contact surface only. A distinct difference between our results and those from previous studies on vesicles is that the F–B phase appears only if the shear elasticity of the RBC spectrin network is small enough, as shown in Fig. 7(c). Therefore, such a phase cannot be observed for RBC doublets, because they have significant shear elasticity.

Fig. 7(b) shows that by increasing the adhesion strength, the contact area exhibits two discontinuous jumps for a fixed μ. The first jump in A_c at very low $\gamma \lesssim 1$ occurs when the adhesion interaction overcomes membrane thermal fluctuations and cell diffusion. The second discontinuity in A_c manifests a transition when one or both RBCs lose their original biconcave shape by forming suddenly a larger contact area in a doublet. For example, it happens when F–B, S–B, and M–F shapes are first attained for $1 < \gamma < 10$, such that a larger contact area is rapidly formed. Interestingly, further transitions with increasing γ (e.g. to the Yin–Yang phase) are continuous, since the contact area is continuously increased with an increase in adhesion strength. Thus, buckling out of a membrane dimple and rapid formation of a larger area of contact can be considered as signatures of a discontinuous transition. An increase in shear elasticity generally delays this discontinuous transition in terms of γ and reduces the contact area, as can be seen in Fig. 7(b) and Movie S2 (ESI†). These results are qualitatively consistent with a discontinuity in A_c found for vesicle doublets.[19]

Since the shear elasticity of membranes has a significant effect on the doublet configurations, the stress-free shape of RBCs might also play an important role in determining the shape of RBC membranes and their doublet phases. Whether the spectrin network of a RBC is stress-free in the biconcave or spherical shape or something in-between is still under debate.[64–67]

So far in this work, the RBCs were stress-free in their biconcave shape. In order to study the effect of the stress-free state of RBCs on doublet phases, the stress-free biconcave shape is compared with a case where the network is stress-free at a deflated sphere shape with eccentricity 0.94. The change in the configuration of the doublets is appreciable, as shown in Fig. 8(b). The most important difference between the two cases is the change of the S–B phase to the M–F phase at small adhesion strengths. If the stress-free shape of RBCs is close to a sphere, the change to the Yin–Yang phase occurs at slightly lower adhesion strengths in comparison to the biconcave stress-free shape, as shown in Fig. 8(b). In practice, this small change cannot be detected experimentally, not only because of the lack of imaging precision, but also because of the natural variance in the mechanical properties of RBC membranes and their reduced volumes.[68,69] As discussed above, the transition from the original biconcave shape of both RBCs to a doublet shape with a large contact area (*e.g.* F–B, S–B, and M–F shapes) is discontinuous in A_c for the biconcave stress-free shape, see Fig. 7(b) and 8(a). Fig. 8(a) also demonstrates that this transition is discontinuous in A_c for the stress-free shape of 0.94.

Strong changes in RBC shapes (*e.g.* for a Yin–Yang doublet) likely lead to appreciable local in-plane deformations of the cell membranes. At the contact area, it is intuitive to expect that RBC membranes are compressed due to adhesive interactions, while the free surfaces are presumably subject to area expansion. These modes of deformation are mainly controlled by the area-compression modulus of a membrane. The area-compression modulus in our model is equal to $2G + k_l + k_a$, where G is the shear modulus and the other terms correspond to local and global

area-conservation constraints. Here, $k_l \approx G$, while $k_a \gg G$ such that the local area constraint leads to rather slight enhancement of the area-compression modulus. Therefore, under strong enough deformations, the local area of a membrane should experience appreciable deformation.

In order to elucidate local strains, local area changes, and the role of the local area constraint, we present in Fig. 9 a comparison of local membrane deformations for a Yin–Yang doublet ($\gamma \approx 85$ and $\mu = 80$) using a RBC model with and without the local area constraint. Fig. 9(c) confirms that the membranes are compressed at the contact area and expanded at the free surfaces. This is also seen in the bimodal distributions of bond and local-area strains in Fig. 9(a) and (b). Here, the bimodality in the local area arises from the differences between adhered and free parts of the membrane. The bimodality in the bond lengths is related to the positive Poisson ratio of our elastic network model, which implies that stretching in one direction is accompanied by compression in the orthogonal direction. The local strains remain approximately within the range $[-0.3, 0.3]$ and their absolute values are slightly smaller for the case with the local area constraint in comparison to that without this constraint. However, in both cases Yin–Yang doublets are observed and their shapes are visually indistinguishable. Thus, for the employed strength of the local area constraint, it plays at most a secondary role in
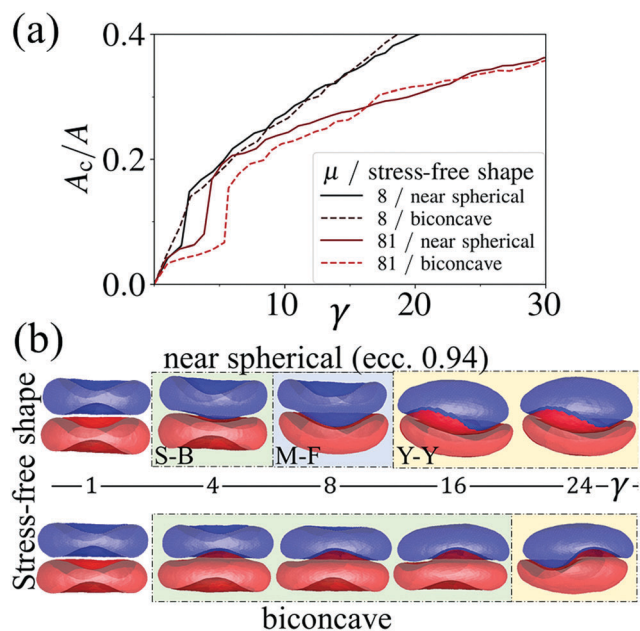

Fig. 8 Effect of the stress-free shape of RBCs on doublet phases for $\nu_1 = \nu_2 = 0.64$. (a) Contact area as a function of γ for biconcave and near spherical (with eccentricity 0.94) stress-free shapes. (b) The shapes of RBC doublets for $\mu = 81$, showing appreciable differences for the two stress-free shapes. The boundaries between different shapes are drawn schematically to guide the eye.
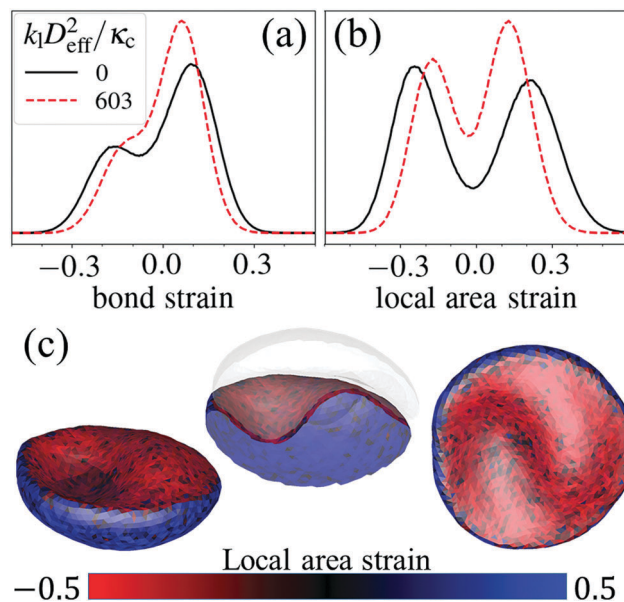

Fig. 9 Effect of the local area constraint in the membrane model on a Yin–Yang doublet for $\gamma \approx 85$, $\mu = 80$, and $\nu_1 = \nu_2 = 0.64$. (a) Bond strain distributions from simulations with and without a local area constraint. The bond strain is defined as $l/l_0 - 1$, where l is the length of a deformed bond and l_0 is its corresponding equilibrium length. (b) Distributions of local triangular area strains. The area strain is defined as $A/A_0 - 1$, where A is the area of a deformed triangle in the spring network and A_0 is its imposed area at the biconcave equilibrium shape. (c) Distribution of local area strains on RBCs within a Yin–Yang doublet. The RBC membranes show a compressive deformation (or negative area strains) at the contact area and are stretched primarily at the free surfaces characterized by positive area strains.

determining doublet shapes for the range of adhesion strengths studied here.

4 Comparison with experiments

The experimental images of the different phases are compared to the simulation results in Fig. 10. The F–B phase is not observed in experiments and not predicted by simulations for the physiological reduced volumes of RBCs. Both in simulations and experiments, M–F doublets form when the adhesion strength is intermediate and the reduced volume is small. The Yin–Yang phase appears when the adhesion strength is high. The S–B phase is seen as a transition state between these two phases. The F–B phase has not been observed in experiments. The F–C phase occurs when both RBCs are swollen and the sheath phase happens when there is a significant difference in the reduced volumes of the two RBCs. To see the F–C phase in experiments, the osmolality of the solution has to increase about two-fold. For increasing the reduced volume of RBCs in experiments, they were immersed in a hypotonic solution of NaCl.

At low shear rates, RBCs aggregate in stacks known as rouleaux.[1,2] The rouleaux increase substantially the viscosity of blood at low shear rates.[6-8] The nucleation of rouleaux starts from RBC doublets. While some doublet structures allow for large rouleau formation, others prevent the formation of large rouleaux. Among all the doublet phases, the M–F and S–B phases allow the RBCs to form large rouleaux with a straight (linear) structure. However, the Yin–Yang phase prevents long straight structures from appearing. Thus, the size of rouleaux in a solution of RBCs depends on their adhesion strength which is determined by the concentration of different adhesive factors in the solution (*e.g.* dextran, fibrinogen). Fig. 11 shows several experimental and simulated results of different rouleau structures. The shapes of rouleaux for high adhesive strengths are very different, depending on the reduced volumes of the RBCs and the number of RBCs in the rouleau. In contrast, the M–F and S–B phases should allow the size of straight rouleau structures to increase with no limit. Note that at high enough adhesive strengths, more complex RBC aggregate structures, other than straight rouleaux, may appear.[70]

The limit for rouleau nucleation can be explained by the free energy of the whole system. Doublet formation changes the free energy of the system by $2E_{def} - \Gamma A_c$. E_{def} is the deformation energy of a RBC, mostly due to bending rigidity and shear elasticity. In principle, it is always positive since any deviation from the equilibrium biconcave shape of a RBC must have
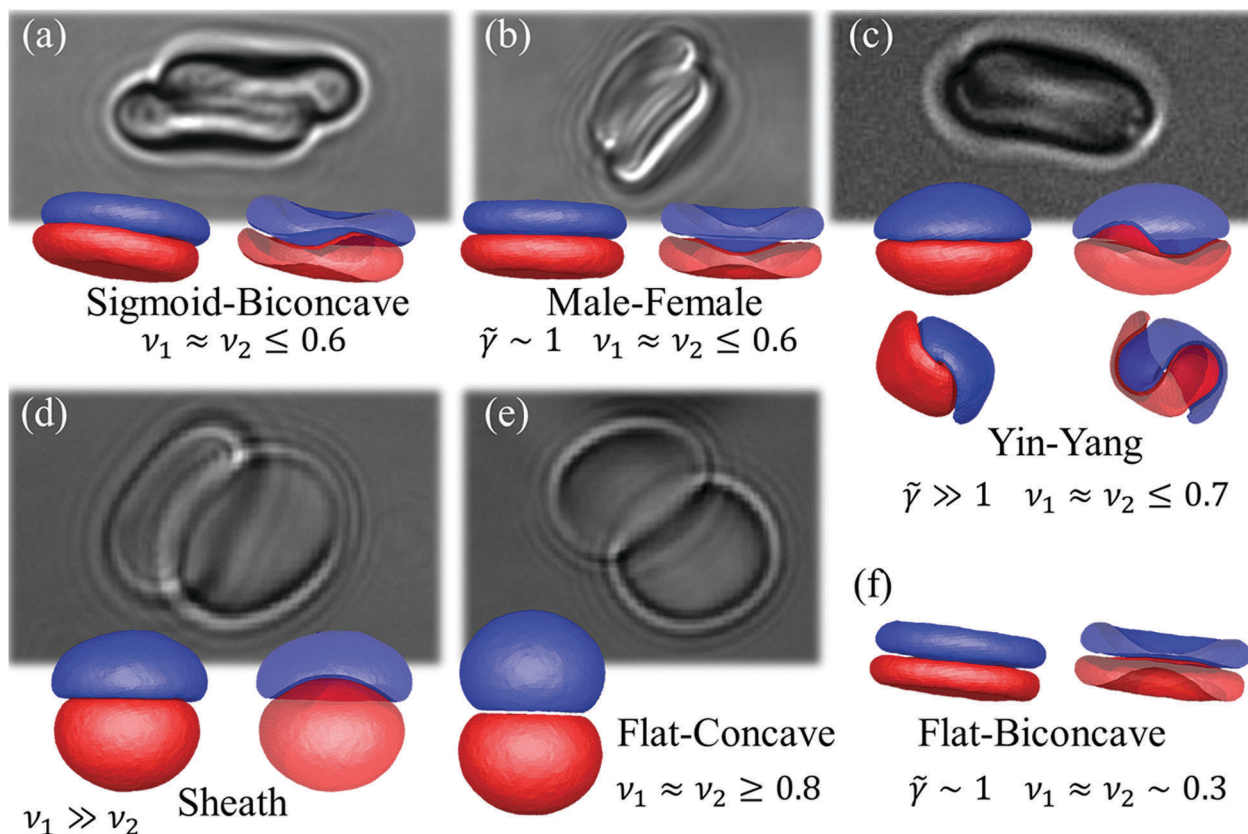
Fig. 10 Comparison of experimental and simulated RBC doublet shapes determined by the adhesion strength, bending modulus, and the reduced volume of RBCs. For simulations, the side and section views are presented for each case. The phases (a) sigmoid–biconcave, (b) male–female, (c) sigmoid–concave (Yin–Yang), (d) sheath, (e) flat–concave, and (f) flat–biconcave are shown. The sheath, F–C, and F–B phases are not probable for RBC doublets under physiological conditions.
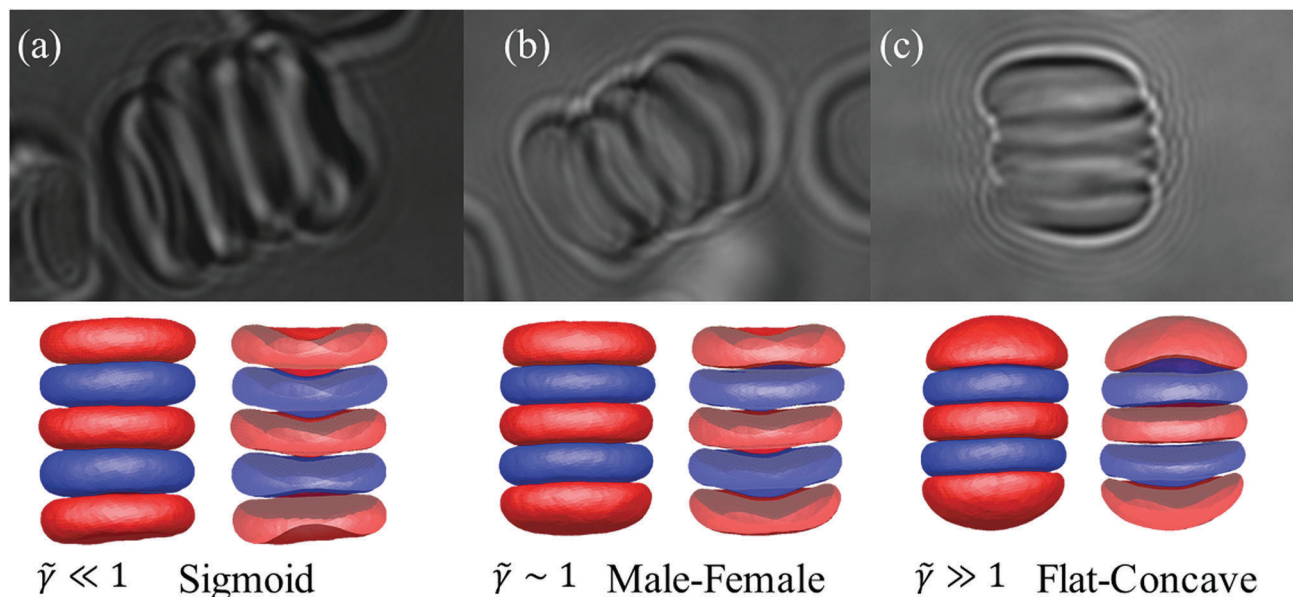
Fig. 11 Various rouleau phases in experiments and simulations. The doublet S–B and M–F phases impose no limit on the size of the rouleau. However, the F–C rouleaux are strongly dependent on the number of interacting RBCs and their reduced volumes. The nucleation point of a F–C rouleau is a Yin–Yang doublet.

a higher energy. Therefore, the adhesion energy ΓA_c must be larger than $2E_{\text{def}}$ for doublet formation to be favorable. Addition of one more RBC to the doublet to make a triplet aggregate of RBCs increases the total free energy by $\Delta E_+ = E_{\text{def}} - \Gamma A_c + E_{\text{def}}^{\text{o}}$, where $E_{\text{def}}^{\text{o}}$ is the additional deformation energy of the original aggregate, E_{def} is the deformation energy of the newly added RBC to the original aggregate and $-\Gamma A_c$ is the adhesion energy due to it. Assuming that the other RBCs in the aggregate do not deform substantially leads to $E_{\text{def}}^{\text{o}} \approx 0$; otherwise, the deformation and adhesion energy of all RBCs must be considered in the rearranged configuration. This rearranged configuration has definitely a higher energy for the RBCs already in the aggregate, since they get away from their equilibrium configuration. For S–B and M–F phases, addition of an RBC to the aggregate adds a constant negative ΔE_+ to the free energy so that the growth of the rouleau is energetically favorable. ΔE_+ is nearly constant since the contact area and curvature of the newly added RBC is similar to the other RBCs in the aggregate. On the contrary, ΔE_+ grows as a new RBC is added to a Yin–Yang doublet, because the contact area for the new RBC is less than the contact area of a doublet, and the new RBC deforms much more in order to fit to the concave shape of a rouleau. As a result, ΔE_+ becomes positive at some point preventing more RBCs from adhering to the aggregate. This limiting point occurs for larger cluster sizes as the adhesion strength Γ increases.

5 Conclusion

A systematic study of RBC doublet formation has been performed. The model employs a triangulated membrane with a polymerized mesh as a representation of the spectrin network. The simulation results demonstrate various doublet phases, namely, the male–female, sigmoid–biconcave, Yin–Yang, sheath, flat–concave, and flat–biconcave phases, with their stability determined by the adhesion strength between two membranes and the reduced volume of each RBC. The male–female phase implies a curved contact area of two RBCs similar to a female–male socket connection. The sigmoid–biconcave phase refers to the condition that two RBCs make a sigmoid S-shape contact while they keep their biconcave curvature. The Yin–Yang phase, then, refers to the same condition, but when the free surfaces of RBCs swell or bend to a concave form. The section view of the doublets in this phase looks like Yin–Yang symbol. The sheath phase occurs when one RBC is swollen so that the other RBC makes a sheath by contacting with it. The flat–concave phase is referred to the flat contact area case and occurs mostly when both RBCs are swollen. The predicted phases are compared with the experimental images obtained from optical imaging of RBCs in different solutions.

The RBC doublet phases are mainly defined by the interplay of the bending energy and the adhesion energy, and are closely related to the reduced volume of RBCs, which is a dimensionless ratio between the volume and the area of RBCs. However, the shear elasticity of the RBC membranes, due to the spectrin network beneath their lipid bilayers, affects their doublet phases. At very low shear moduli, the flat–biconcave shape appears at low adhesion strengths, while this phase is never stable for healthy RBCs with normal shear moduli. The very peculiar flat–concave phase at the normal reduced volumes of RBCs is also reported for very low shear moduli. This shows that the spectrin network's shear elasticity is a key player in defining the RBC doublet phases, differentiating them from previously studied fluid vesicle doublets.

Rouleau nucleation depends on how RBCs make doublets first. Aggregation of RBCs always brings a rise in the bending free energy and a decrease in the adhesive energy. Depending on the doublet shape, this pair of energy-changes determines whether rouleau formation is allowed or not. As a result, at high adhesion strengths, the doublets tend to prevent large stacks, since the Yin–Yang phase makes the positive change of the bending energy so large that it cannot be compensated for by the adhesion energy related to the contact area of the membranes. At low and moderate adhesion strengths, the sigmoid–biconcave and male–female phases allow the growth of the rouleaux, since the addition of a RBC to the aggregate does not change the shapes of the other RBCs, which have already adhered to the aggregate. These results can be used for determining the adhesion strength and membrane properties of healthy and diseased RBCs.

Conflicts of interest

There are no conflicts to declare.

Acknowledgements

Notes and references

1 E. W. Merrill, E. R. Gilliland, T. S. Lee and E. W. Salzman, *Circ. Res.*, 1966, **18**, 437–446.
2 S. Chien, S. Usami, R. J. Dellenback and M. I. Gregersen, *Am. J. Physiol.*, 1970, **219**, 143–153.
3 H. Bäumler, B. Neu, E. Donath and H. Kiesewetter, *Biorheology*, 1999, **36**, 439–442.
4 B. Neu and H. J. Meiselman, *Biophys. J.*, 2002, **83**, 2482–2490.
5 B. Neu, R. Wenby and H. J. Meiselman, *Biophys. J.*, 2008, **95**, 3059–3065.
6 E. W. Merrill, E. R. Gilliland, G. Cokelet, H. Shin, A. Britten and R. E. Wells Jr., *Biophys. J.*, 1963, **3**, 199–213.
7 S. Chien, S. Usami, H. M. Taylor, J. L. Lundberg and M. I. Gregersen, *J. Appl. Physiol.*, 1966, **21**, 81–87.
8 R. Skalak, S. R. Keller and T. W. Secomb, *J. Biomech. Eng.*, 1981, **103**, 102–115.
9 W. Helfrich, *Z. Naturforsch., C: J. Biosci.*, 1973, **28**, 693–703.
10 H. J. Deuling and W. Helfrich, *Biophys. J.*, 1976, **16**, 861–868.
11 R. Lipowsky, *Nature*, 1991, **349**, 475–481.
12 U. Seifert, *Adv. Phys.*, 1997, **46**, 13–137.
13 Y. C. Fung, *Biomechanics: Mechanical properties of living tissues*, Springer-Verlag, New York, 2nd edn, 1993.
14 G. H. W. Lim, M. Wortis and R. Mukhopadhyay, *Proc. Natl. Acad. Sci. U. S. A.*, 2002, **99**, 16766–16769.
15 N. Gov, A. G. Zilman and S. Safran, *Phys. Rev. Lett.*, 2003, **90**, 228101.
16 R. Skalak, P. R. Zarda, K.-M. Jan and S. Chien, *Biophys. J.*, 1981, **35**, 771–781.
17 R. Skalak and S. Chien, *Ann. N. Y. Acad. Sci.*, 1983, **416**, 138–148.
18 S. Chien, L. A. Sung, S. Simchon, M. M. L. Lee, K.-M. Jan and R. Skalak, *Ann. N. Y. Acad. Sci.*, 1983, **416**, 190–206.
19 P. Ziherl and S. Svetina, *Proc. Natl. Acad. Sci. U. S. A.*, 2007, **104**, 761–765.
20 S. Svetina and P. Ziherl, *Bioelectrochemistry*, 2008, **73**, 84–91.
21 R. Gu, X. Wang and M. Gunzburger, *J. Math. Biol.*, 2016, **73**, 1293–1319.
22 P. Bagchi, P. C. Johnson and A. S. Popel, *J. Biomech. Eng.*, 2005, **127**, 1070–1080.
23 J. Zhang, P. C. Johnson and A. S. Popel, *J. Biomech.*, 2008, **41**, 47–55.
24 M. Ju, S. S. Ye, H. T. Low, J. Zhang, P. Cabrales, H. L. Leo and S. Kim, *Phys. Biol.*, 2013, **10**, 036001.
25 D. Flormann, O. Aouane, L. Kaestner, C. Ruloff, C. Misbah, T. Podgorski and C. Wagner, *Sci. Rep.*, 2017, **7**, 7928.
26 Q. Yu, S. Othman, S. Dasgupta, T. Auth and G. Gompper, *Nanoscale*, 2018, **10**, 6445–6458.
27 J. Li, M. Dao, C. T. Lim and S. Suresh, *Biophys. J.*, 2005, **88**, 3707–3719.
28 D. A. Fedosov, B. Caswell and G. E. Karniadakis, *Comput. Meth. Appl. Mech. Eng.*, 2010, **199**, 1937–1948.
29 D. A. Fedosov, B. Caswell and G. E. Karniadakis, *Biophys. J.*, 2010, **98**, 2215–2225.
30 Z. Wu, Z. Xu, O. Kim and M. Alber, *Philos. Trans. R. Soc., A*, 2014, **372**, 20130380.
31 E. A. Evans, *Biophys. J.*, 1974, **14**, 923–931.
32 G. Gompper and D. M. Kroll, *J. Phys.*, 1996, **6**, 1305–1320.
33 F. Jülicher, *J. Phys.*, 1996, **6**, 1797–1824.
34 G. Gompper and D. M. Kroll, *J. Phys.: Condens. Matter*, 1997, **9**, 8795–8834.
35 Y. Kantor and D. R. Nelson, *Phys. Rev. A: At., Mol., Opt. Phys.*, 1987, **36**, 4020–4032.
36 D. H. Boal and M. Rao, *Phys. Rev. A: At., Mol., Opt. Phys.*, 1992, **46**, 3037–3045.
37 J. Lidmar, L. Mirny and D. R. Nelson, *Phys. Rev. E: Stat., Nonlinear, Soft Matter Phys.*, 2003, **68**, 051910.
38 H. Turlier, D. A. Fedosov, B. A. Audoly, T. Auth, N. S. Gov, C. Sykes, J.-F. Joanny, G. Gompper and T. Betz, *Nat. Phys.*, 2016, **12**, 513–519.
39 L. Lanotte, J. Mauer, S. Mendez, D. A. Fedosov, J.-M. Fromental, V. Claveria, F. Nicoud, G. Gompper and M. Abkarian, *Proc. Natl. Acad. Sci. U. S. A.*, 2016, **113**, 13289–13294.
40 D. A. Fedosov, M. Peltomäki and G. Gompper, *Soft Matter*, 2014, **10**, 4258–4267.
41 A. Guckenberger, M. P. Schraml, P. G. Chen, M. Leonetti and S. Gekle, *Comput. Phys. Commun.*, 2016, **207**, 1–23.

42 A. Guckenberger and S. Gekle, *J. Phys.: Condens. Matter*, 2017, **29**, 203001.

43 G. Gompper and D. M. Kroll, *Statistical mechanics of membranes and surfaces*, World Scientific, Singapore, 2nd edn, 2004, pp. 359–426.

44 P. B. Canham, *J. Theor. Biol.*, 1970, **26**, 61–81.

45 E. A. Evans and R. Skalak, *Mechanics and thermodynamics of biomembranes*, CRC Press, Inc., Boca Raton, Florida, 1980.

46 R. Waugh and E. A. Evans, *Biophys. J.*, 1979, **26**, 115–131.

47 H. Strey, M. Peterson and E. Sackmann, *Biophys. J.*, 1995, **69**, 478–488.

48 S. Henon, G. Lenormand, A. Richert and F. Gallet, *Biophys. J.*, 1999, **76**, 1145–1151.

49 S. Suresh, J. Spatz, J. P. Mills, A. Micoulet, M. Dao, C. T. Lim, M. Beil and T. Seufferlein, *Acta Biomater.*, 2005, **1**, 15–30.

50 H. S. Seung and D. R. Nelson, *Phys. Rev. A: At., Mol., Opt. Phys.*, 1988, **38**, 1005–1018.

51 M. Dao, J. Li and S. Suresh, *Mater. Sci. Eng., C*, 2006, **26**, 1232–1244.

52 M. P. Allen and D. J. Tildesley, *Computer simulation of liquids*, Clarendon Press, New York, 1991.

53 U. Seifert, K. Berndl and R. Lipowsky, *Phys. Rev. A: At., Mol., Opt. Phys.*, 1991, **44**, 1182–1202.

54 D. Yoon and D. You, *J. Biomech.*, 2016, **49**, 2267–2279.

55 M. A. Peterson, *Phys. Rev. A: At., Mol., Opt. Phys.*, 1992, **45**, 4116–4131.

56 Y.-K. Park, C. A. Best, T. Auth, N. S. Gov, S. A. Safran, G. Popescu, S. Suresh and M. S. Feld, *Proc. Natl. Acad. Sci. U. S. A.*, 2010, **107**, 1289–1294.

57 A. A. Evans, B. Bhaduri, G. Popescu and A. J. Levine, *Proc. Natl. Acad. Sci. U. S. A.*, 2017, **114**, 2865–2870.

58 O. K. Baskurt, M. Boynard, G. C. Cokelet, P. Connes, B. M. Cooke, S. Forconi, F. Liao, M. R. Hardeman, F. Jung, H. J. Meiselman, G. Nash, N. Nemeth, B. Neu, B. Sandhagen, S. Shin, G. Thurston and J. L. Wautier, *Clin. Hemorheol. Microcirc.*, 2009, **42**, 75–97.

59 P. Steffen, C. Verdier and C. Wagner, *Phys. Rev. Lett.*, 2013, **110**, 018102.

60 M. Brust, O. Aouane, M. Thiébaud, D. Flormann, C. Verdier, L. Kaestner, M. W. Laschke, H. Selmi, A. Benyoussef, T. Podgorski, G. Coupier, C. Misbah and C. Wagner, *Sci. Rep.*, 2014, **4**, 4348.

61 K. Buxbaum, E. Evans and D. E. Brooks, *Biochemistry*, 1982, **21**, 3235–3239.

62 M. Puig-de-Morales-Marinkovic, K. T. Turner, J. P. Butler, J. J. Fredberg and S. Suresh, *Am. J. Physiol.*, 2007, **293**, C597–C605.

63 M. Diez-Silva, M. Dao, J. Han, C.-T. Lim and S. Suresh, *MRS Bull.*, 2010, **35**, 382–388.

64 T. M. Fischer, C. W. M. Haest, M. Stöhr-Liesen, H. Schmid-Schönbein and R. Skalak, *Biophys. J.*, 1981, **34**, 409–422.

65 B. Daily, E. L. Elson and G. I. Zahalak, *Biophys. J.*, 1984, **45**, 671–682.

66 T. Švelc and S. Svetina, *Cell. Mol. Biol. Lett.*, 2012, **17**, 217–227.

67 D. Cordasco, A. Yazdani and P. Bagchi, *Phys. Fluids*, 2014, **26**, 041902.

68 P. B. Canham and A. C. Burton, *Circ. Res.*, 1968, **22**, 405–422.

69 G. B. Nash and S. J. Wyard, *Biochim. Biophys. Acta*, 1981, **643**, 269–275.

70 R. W. Samsel and A. S. Perelson, *Biophys. J.*, 1982, **37**, 493–514.